PCCP

PAPER

View Article Online
View Journal | View Issue

Cite this: *Phys. Chem. Chem. Phys.*, 2015, **17**, 19261

Device characterization and optimization of small molecule organic solar cells assisted by modelling simulation of the current–voltage characteristics†

Yi Zuo, Xiangjian Wan,* Guankui Long, Bin Kan, Wang Ni, Hongtao Zhang and Yongsheng Chen*

Received 14th May 2015,
Accepted 19th June 2015

DOI: 10.1039/c5cp02783g

www.rsc.org/pccp

In order to understand the photovoltaic performance differences between the recently reported DR3TBTT-HD and DR3TBDT2T based solar cells, a modified two-diode model with Hecht equation was built to simulate the corresponding current–voltage characteristics. The simulation results reveal that the poor device performance of the DR3TBDTT-HD based device mainly originated from its insufficient charge transport ability, where an average current of 5.79 mA cm^{-2} was lost through this pathway at the maximum power point for the DR3TBDTT-HD device, nearly three times as large as that of the DR3TBDT2T based device under the same device fabrication conditions. The morphology studies support these simulation results, in which both Raman and 2D-GIXD data reveal that DR3TBTT-HD based blend films exhibit lower crystallinity. Spin coating at low temperature was used to increase the crystallinity of DR3TBDTT-HD based blend films, and the average current loss through insufficient charge transport at maximum power point was suppressed to 2.08 mA cm^{-2}. As a result, the average experimental power conversion efficiency of DR3TBDTT-HD based solar cells increased by over 40%.

Introduction

Organic photovoltaics (OPV) are thought of as an alternative to traditional silicon solar cells because of their attractive advantages, such as low cost, light weight and potential application in flexible devices.[1–6] In the past few years, solution-processable organic bulk heterojunction (BHJ) solar cells have made remarkable progress. Both polymer based organic photovoltaics (P-OPV) and small molecule based organic photovoltaics (SM-OPV) have achieved power conversion efficiencies (PCE) of around 10% in single-junction BHJ solar cells.[7–11] However, further improving the PCE is still urgently required for its viable application.[11–14]

A photovoltaic device is ultimately an electrical device with numerous current loss mechanisms inside. Compared with Si based devices, the lower current at maximum power point (MPP) of OPV devices is one of the main hampering factors that lead to their lower performance. The reasons for the lower current could include insufficient charge generation and large current loss. Hence, figuring out these current losses and then finding a way to suppress them are of great value to achieve better OPV performance.[15–17] However, an OPV device is much like a black box and we know little about it except for its current–voltage (*J–V*) characteristics. Herein, formulating equations in terms of semiconductor theory to simulate the current–voltage characteristics is a very useful way to reveal these current losses.[18–20] So far several models, such as the one-diode model,[19] the two-diode model,[21] the three-diode model,[22] and many other models,[23–25] have been built to describe various photovoltaic systems.

In our previous work, we reported two small molecules for photovoltaic applications named DR3TBDTT-HD and DR3TBDT2T (Fig. 1) with the same backbone structure but a slight difference in the side chain on the BDT unit.[26] These two compounds have similar energy levels and optical band-gaps

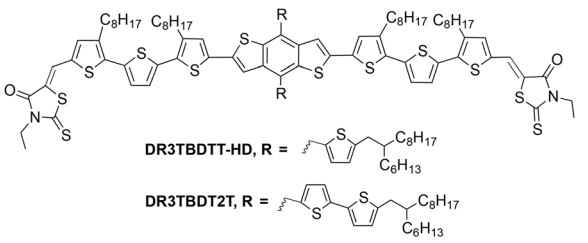

Fig. 1 Chemical structures of compounds DR3TBDTT-HD and DR3TBDT2T.

Key Laboratory of Functional Polymer Materials and Centre for Nanoscale Science and Technology, Collaborative Innovation Center of Chemical Science and Engineering, Nankai University, Tianjin 300071, China.
E-mail: xjwan@nankai.edu.cn, yschen99@nankai.edu.cn

† Electronic supplementary information (ESI) available: Values of experimental and model simulation parameters, results of independent samples *t*-test. See DOI: 10.1039/c5cp02783g

(Table S1, ESI†), but the photovoltaic performances of their corresponding devices are quite different and the performance of the DR3TBDTT-HD based device was much poorer than that of the DR3TBDT2T-based device. Thus, it would be very helpful for future OPV engineering to figure out the reasons for the performance difference. In this work, batches of new photovoltaic devices with a simple structure of ITO/PEDOT:PSS/active layer/Al were fabricated to study this issue. A classical 2-diode model was firstly used to simulate the *J–V* characteristics curves, but it was found that our system was too complex for this classical model. Then, this classical model was modified by Hecht equation and the modified model could simulate the experimental *J–V* curves. The simulation result reveals that the poor performance of the DR3TBDTT-HD based devices was due to their large leakage current at MPP that originated from the insufficient charge transport ability. The morphology studies supported our simulation results, that DR3TBTT-HD based blend films exhibit a lower crystallinity, which is bad for charge transport. Thus, using this information, the devices based on DR3TBDTT-HD were fabricated at a lower temperature to increase the charge transport ability and reduce the current losses, which significantly improved the average PCE by over 40%.

Experimental section

Materials and solar cell fabrication

[6,6]-Phenyl-C_{71}-butyric acid methyl ester ($PC_{71}BM$) was purchased from American Dye Source, Inc. Polydimethylsiloxane, trimethylsiloxy terminated (PDMS, M_W 14 000) was purchased from Alfa Aesar Inc. Compounds DR3TBDTT-HD and DR3TBDT2T were prepared according to the literature.[26]

The devices were fabricated with a simple structure of glass/ITO/PEDOT:PSS/active layer/Al. The ITO-coated glass substrates were cleaned by ultrasonic treatments in detergent, deionized water, acetone, and isopropyl alcohol under ultra-sonication for 15 minutes each and subsequently dried by a nitrogen blow. A thin layer of PEDOT:PSS (Clevios P VP AI 4083, filtered at 0.45 μm) was spin-coated at 3000 rpm onto an ITO surface. After baking at 150 °C for 20 minutes, the substrates were transferred to an argon-filled glove box. The active layer was spin-coated from $CHCl_3$ solution with 0.2 mg mL^{-1} PDMS. The donor : $PC_{71}BM$ ratio is 1 : 0.8 and the donor concentration is 10 mg mL^{-1}. Finally, an 80 nm Al layer was deposited under high vacuum ($<2 \times 10^{-4}$ Pa) and the evaporation rate was <0.01 nm in the first 1 nm. The effective area of cells was 4 mm^2 as defined by shallow masks. For temperature control, 15 °C was obtained by central air-conditioning, and 0–5 °C was obtained by placing cooling boxes into the glove box.

Characterization

The current–voltage characteristics of the photovoltaic devices were obtained by using a Keithley 2400 source-measure unit. The photocurrent was measured under simulated illumination of 100 mW cm^{-2} AM 1.5G irradiation using an Oriel 96 000 solar simulator, calibrated with a standard Si solar cell.

The thicknesses of the active layer in the photovoltaic devices were measured on a VeecoDektak 150 profilometer.

The SCLC hole-only mobility was measured using a diode configuration with the ITO/PEDOT:PSS/active layer/Au device structure by taking the dark current density in the effective voltage range of 0–4 V. By non-linear fitting the corresponding *J–V* characteristics to a space charge limited form, we obtained the mobility results, where SCLC is described by equation: $J = \left(9\varepsilon_0\varepsilon_r\mu_0 {V_{\text{eff}}}^2\right)/\left\{8L^3\exp\left(0.89\beta\sqrt{V_{\text{eff}}/L}\right)\right\}$, where J is the current density, L is the film thickness of the active layer, μ_0 is the hole or electron mobility, ε_r is the relative dielectric constant of the transport medium, ε_0 is the permittivity of free space (8.85×10^{-12} F m^{-1}), and $V_{\text{eff}}(V_{\text{appl}} - V_{\text{bi}})$ is the effective voltage in the device, where V_{appl} is the applied voltage to the device and V_{bi} is the built-in voltage due to the relative work function difference of the two electrodes.

Raman samples were prepared on PEDOT:PSS-coated ITO substrates using the same preparation conditions as for photovoltaic devices. Spectra were examined with a LabRAM HR Raman spectrometer using laser excitation at 633 nm.

Two-dimensional (2D) grazing incidences wide-angle X-ray diffraction (GI-WAXD) samples were prepared on PEDOT:PSS-coated Si substrates using the same preparation conditions as for the photovoltaic devices. The data were obtained with an area CCD detector of 3072 by 3072 pixels resolution (225 mm by 225 mm) at Beamline BL14B1 of the Shanghai Synchrotron Radiation Facility (SSRF). The monochromatic energy of the X-ray source was 10 keV. The X-ray wavelength was 1.2378 Å and the incidence angle was 0.2°.

Results and discussion

Photovoltaic performance

SM-OPV devices were fabricated for compounds DR3TBDTT-HD and DR3TBDT2T, and the performances of all the devices are summarized in Tables S2 and S3 (ESI†). The average experimental PCEs of the DR3TBDTT-HD and DR3TBDT2T based devices were 5.63% and 8.02%, respectively. For the comparison between samples, it is necessary to utilize statistical methods. After carrying out the Independent Samples *t*-test, we found that there is significant difference between the average PCEs of the DR3TBDTT-HD and DR3TBDT2T based devices (Table S4, ESI†), which confirmed that the device performance of DR3TBDTT-HD based devices is poorer.

$$\text{PCE} = \frac{J_{\text{mp}}V_{\text{mp}}}{P_{\text{in}}} = \frac{V_{\text{oc}}J_{\text{sc}}\text{FF}}{P_{\text{in}}} \quad (1)$$

In order to figure out the differences in their performance, model simulation was used to analyse their corresponding *J–V* characteristics. As defined by eqn (1),[27] under standard illumination (P_{in} = 100 mW cm^{-2}), PCE is the product of current (J_{mp}) times voltage (V_{mp}) at MPP. Device parameters of open circuit voltage (V_{oc}) and short circuit current (J_{sc}) are two special data points in the *J–V* curve: the open circuit point and the short circuit point, respectively. If we could formulate an equation in

terms of theory to simulate all the data points of the *J–V* curves, we would be able to build a deeper understanding of these solar cells according to the simulation parameters.

Model simulating

In the first place, a model that is suitable for our SM-OPV devices should be built. According to semiconductor theory, there is a classical two-diode model to describe the *J–V* characteristics of a photovoltaic device: diode D_1 with an ideal factor of 1 attributed to the diffusion current, and diode D_2 with an ideal factor of 2 attributed to the recombination current.[28,29] The equivalent circuit is presented in Fig. 2a and the corresponding equations are as below:[30–33]

$$J = -J_{ph} + J_{diode} + J_{leak} \quad (2)$$

$$J_{diode} = J_1\left[\exp\left(q\frac{V - JR_S}{k_B T}\right) - 1\right] + J_2\left[\exp\left(q\frac{V - JR_S}{2k_B T}\right) - 1\right] \quad (3)$$

$$J_{leak}{}' = \frac{V - JR_S}{R_p} \quad (4)$$

In eqn (2)–(4), J is the output current, V is the output voltage, J_{diode} is the current losses through the heterojunction interface, $J_{leak}{}'$ is the current leakage through the parasitic circuit with a resistance of R_P, and J_{ph} is the saturation photo-generated current at the donor–acceptor interface, which is also written as $J_{ph,sat}$ or J_{ph}^{sat} in some other works.[34,35] k_B is the Boltzmann constant, T is the absolute temperature, and q is the absolute value of electron charge. J_1 and J_2 are the reverse saturation currents of D_1 and D_2, respectively. R_S is the equivalent series resistance including electrode resistance, bulk resistance of the organic semiconductor, and Ohmic contact resistance of the metal-semiconductor contact. In this model, the parasitic circuit is originated from the short circuit channels caused by imperfect device fabrication process and R_P is a fixed value resistance that has a linear response with terminal voltage.

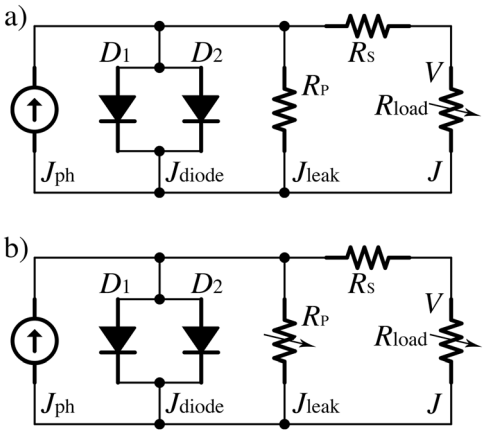

Fig. 2 (a) Equivalent circuit of a classical two-diode model under illumination. Its R_P is a fixed value resistance. (b) Equivalent circuit of a modified two-diode model under illumination. Its R_P is a variable resistance that is a function of V.

R_P can be estimated by the slope of the *J–V* curve near short circuit conditions.[36–38]

Unfortunately, it was found that there are two obstacles preventing the use of the classical two-diode model (Fig. 2a) in our devices. First, though this model could well reconstruct the *J–V* curves of the DR3TBDT2T based cells, it could hardly reconstruct the *J–V* characteristics of the DR3TBDTT-HD based devices. This indicates that for the less-efficient DR3TBDTT-HD based devices, there should be other current loss mechanisms that have not been included in this classical model. Second, the estimated R_P of the devices under standard illumination (no more than 1 kohm cm^2) is at least one order of magnitude less than those in the dark (more than 10 kohm cm^2). The same phenomenon was also observed by other groups whereby the R_P will decrease after increasing the illumination intensity.[20,24,39] This phenomenon not only indicates that R_P should not be a fixed value resistance, but also reveals that the current leakage through short-circuit channels is only a small proportion of the total J_{leak}.

Considering there is a charge collection process for the separated charge's transport to the electrode, the Hecht equation was used to modify the leak current item.[40–42] The Hecht equation could describe the current loss in a system with limited mobility-lifetime product.[43–45] Hence, a modified two-diode model with a modified current leakage mechanism was built, in which the leak *J–V* characteristic is presented below:

$$J_{leak} = J_{ph} - J_{ph}C_C V_{eff} \times \left[1 - \exp\left(-\frac{1}{C_C V_{eff}}\right)\right] \quad (5a)$$

$$C_C = \mu\tau / Ld \quad (5b)$$

$$V_{eff} = V_{BI} - (V - JR_S) \quad (5c)$$

where $\mu\tau$ is the mobility-lifetime product, d is the active layer thickness, L is the distance that the carrier needs to travel, and is estimated as $d/2$ in literature.[42] V is the output voltage, and V_{BI} is the built-in voltage, which is estimated by the energy difference between the LUMO energy level of the $PC_{71}BM$ material and the HOMO energy level of the donor material. V_{eff} is the effective voltage for the free charge transport from the donor–acceptor interface to the electrodes. As defined in eqn (5b), C_C refers to the charge collection parameter that describes the charge transport ability, and C_C is a constant for a certain device, which is independent of the test voltage. A simple numeric simulation of eqn (5a) was performed to study the differences and resemblances between old $J_{leak}{}'$ and modified J_{leak}. For common SM-OPV devices, the V_{oc} is often achieved at a V_{eff} of around 0.1 V, the maximum power output point is often achieved at a V_{eff} between 0.3 and 0.5 V, and the J_{sc} is often achieved at a V_{eff} of around 1 V. As shown in Fig. S1 (ESI†), for high C_C devices, the current–voltage response is small and approximate to linear at V_{eff} from V_{oc} point to J_{sc} point. As a result, the modified J_{leak} in the high C_C device can be described by a much simpler formula, such as old $J_{leak}{}'$. But for a lower C_C device, the leak current is larger and exhibits a non-linear relationship with the applied voltage, which could not be described by old $J_{leak}{}'$.

The modified equivalent circuit is present in Fig. 2b. When substituting eqn (3), (5a), and (5c) into eqn (2), the total J–V equation was obtained as below:

$$J = J_1\left[\exp\left(q\frac{V - JR_S}{k_BT}\right) - 1\right] + J_2\left[\exp\left(q\frac{V - JR_S}{2k_BT}\right) - 1\right] - J_{ph}C_C(V_{BI} + JR_S - V) \times \left[1 - \exp\left(-\frac{1}{C_C(V_{BI} + JR_S - V)}\right)\right] \quad (6)$$

Fortunately, this modified model with eqn (6) could simulate the J–V characteristics of both DR3TBDTT-HD and DR3TBDT2T based cells very well. Examples of the simulations for their best device are presented in Fig. 3a. From the simulation parameters, we could reconstruct their corresponding J–V characteristic curves to obtain a simulating PCE. Statistical analysis confirmed (Table S4, ESI†) that there is no significant difference between the average experimental PCE and the average simulating PCE for both DR3TBDTT-HD and DR3TBDT2T based cells.

Simulation result analysis

As shown in Table 1 and Fig. 3b and c, the current losses for the best device were quantitatively analysed to reveal the performance difference between DR3TBDTT-HD and DR3TBDT2T based photovoltaic device. The current losses through diode ($J_{diode,mp}$) and leak current ($J_{leak,mp}$) at MPP can be calculated by eqn (3) and (5) based on the simulation results. As a general understanding, a device with higher V_{oc} and J_{ph} is more likely to have larger V_{mp} and J_{mp}. However, for DR3THDTT-HD's best device, its V_{oc} and J_{ph} are higher than DR3TBDT2T's, while its V_{mp} and J_{mp} are smaller. The main cause for this phenomenon is its J_{leak}. On the one hand, the J_{leak} is growing fast with the output voltage that made its V_{mp} obtained at a lower voltage of 0.71 V. On the other hand, though its J_{ph} is as high as 14.1 mA cm^{-2}, the $J_{leak,mp}$ is too large, which leads to a small J_{mp} of 8.92 mA cm^{-2}. Finally, a smaller V_{mp} and a smaller J_{mp} definitely result in a smaller PCE. For DR3TBDT2T's best device, although its V_{oc} and J_{ph} are lower, due to its small and slow growing J_{leak}, its V_{mp},J_{mp}, and PCE are even larger. It can also be found from Table 1 that the trend of the parameter's average values are in line with the trend of the best values, which indicate that the poor performance of DR3TBDTT-HD based devices was mainly due to its large J_{leak}. As described in eqn (5), a large J_{leak} originates from an insufficient C_C, and C_C refers to the film's charge transport ability. Thus, the lower C_C indicates that the charge transport ability of the DR3TBDTT-HD based film is not enough.

Morphology characterization

In order to find out the reason for the different charge transport abilities between DR3TBDTT-HD and DR3TBDT2T based devices, morphologies of the corresponding active layers were characterized by Raman spectroscopy. A film with higher charge transport ability commonly exhibits a higher phase crystallinity, and a more crystalized phase would exhibit a narrower full width at

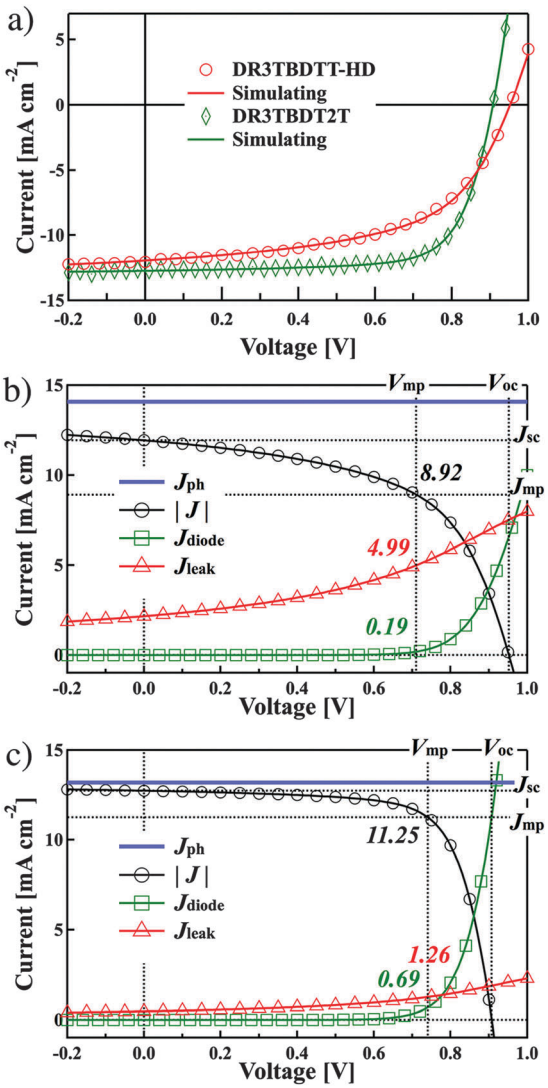

Fig. 3 (a) Simulated J–V curves for devices A13 and H16. Symbols are experimental data and lines are simulated curves. (b) The simulation current of device A13. (c) The simulated currents of device H16. A13 and H16 are the best devices for DR3TBDTT-HD and DR3TBDT2T based cells, respectively.

half maximum (FWHM) of the C=C mode in Raman spectra.[46,47] According to the literature, the vibration bands around 1450 cm^{-1} can be attributed to the C=C stretching vibration of the thiophene ring.[48] As summarized in Table 2, the FWHM of the Raman C=C mode for DR3TBDTT-HD was 28.5 ± 0.4 cm^{-1}, while the DR3TBDT2T based blend films exhibit a narrower FWHM of 24.9 ± 0.5 cm^{-1}. As confirmed by statistical analysis (Table S5, ESI†), it could be concluded that DR3TBDTT-HD based films really have a lower crystallinity.

The Raman result was supported by two-dimensional (2D) grazing incidences wide-angle X-ray diffraction (GI-WAXD) results and SCLC hole mobility data. For the GI-WAXD test, in order to avoid interference from small-angle scattering light, the detector-sample distance was as long as 515 mm, and the (100) peaks of the blend films are well fitted by Gaussian (Fig. S2, ESI†). From Table 2, the peak for the DR3TBDT2T based film is higher and

Table 1 Device simulating parameters for DR3TBDTT-HD and DR3TBDT2T based devices. The best devices for DR3TBDTT-HD and DR3TBDT2T are device A13 and H16, respectively. The average values are calculated from around 20 devices. More detailed data are summarized in Tables S2 and S3 (ESI)

Parameter		PCE [%]	V_{mp} [V]	J_{mp} [mA cm^{-2}]	V_{oc} [V]	J_{ph} [mA cm^{-2}]	C_C	$J_{diode,mp}$ [mA cm^{-2}]	$J_{leak,mp}$ [mA cm^{-2}]
DR3TBDTT-HD	Best	6.34	0.71	8.92	0.952	14.1	2.7	0.19	4.99
	Average	5.66	0.67	8.42	0.960	14.4	2.4	0.23	5.79
DR3TBDT2T	Best	8.33	0.74	11.25	0.907	13.2	12.0	0.69	1.26
	Average	8.01	0.74	10.80	0.911	13.3	8.2	0.59	1.87

Table 2 The morphology data of DR3TBDTT-HD and DR3TBDT2T based blend films is summarized. More detailed data about Raman spectrum and SCLC hole-mobility are summarized in Tables S5 and S6 (ESI), respectively

Compound	Raman FWHM (cm^{-1})	GIWAXD FWHM (nm^{-1})	GIWAXD peak intensity (—)	SCLC (10^{-4} cm^2 V^{-1} s^{-1})
DR3TBDTT-HD	28.5 ± 0.4	0.406	46	1.18 ± 0.24
DR3TBDT2T	24.9 ± 0.5	0.328	90	3.33 ± 0.34

narrower than that of the DR3TBDTT-HD based film, which indicates that the DR3TBDT2T based film has a higher crystallinity and larger crystal size.[49,50] For the SCLC hole mobility of DR3TBDTT-HD based films, as summarized in Table 2, comparing with the high mobility of $3.33 \pm 0.34 \times 10^{-4}$ cm^2 V^{-1} s^{-1} for DR3TBDT2T based devices, the average hole mobility of DR3TBDTT-HD devices is only $1.18 \pm 0.24 \times 10^{-4}$ cm^2 V^{-1} s^{-1}.

The morphology results not only confirmed the insufficient charge transport ability of the DR3TBDTT-HD based films, but also gave an explanation for the large J_{ph} of the DR3TBDTT-HD based devices. Although small crystal size is harmful to charge transport, it is good for photo-generated exciton diffusion to the heterojunction interface, and caused a higher photo-generated free charge. As a result, the average J_{ph} of the DR3TBDTT-HD based devices is 1 mA cm^{-2} higher than that of the DR3TBDT2T based devices (Table 1).

Further device optimization

For the poor-performing DR3TBDTT-HD based device, now that we know its decreased performance resulted from the large C_C caused by insufficient film crystallinity, we decided to increase the C_C to improve its device performance. According to the literature, slowing the solvent evaporation rate and film growth rate could form high crystallinity domains.[8,47,51–55] In addition, reducing the spin-coating temperature could achieve this goal.[8] Therefore, the active layer was spin-coated at a lower temperature and the corresponding films were characterized by Raman spectroscopy. As summarized in Table S7 (ESI†), the FWHM of C=C mode was successfully decreased from 28.5 ± 0.4 cm^{-1} to 26.7 ± 0.2 cm^{-1} and 25.3 ± 0.4 cm^{-1} when spin-coating temperature at 15 °C and 0–5 °C, respectively. These data indicate that decreasing the spin-coating temperature could indeed increase the phase crystallinity.

Inspired by the positive morphology results, new batches of photovoltaic devices were fabricated by low temperature coating. The corresponding *J–V* curves were simulated by eqn (6), and examples of the simulation are presented in Fig. 4a. As confirmed by statistical analysis (Table S4, ESI†), there is no significant difference between the experimental PCEs and the simulating PCEs for the DR3TBDTT-HD based solar cells under different fabrication temperatures. Thus, the simulation parameters were used to analyze the experimental *J–V* curves.

As shown in Fig. 4b and c and Table 3, for the best DR3TBDTT-HD based devices, after decreasing the spin-coating temperature

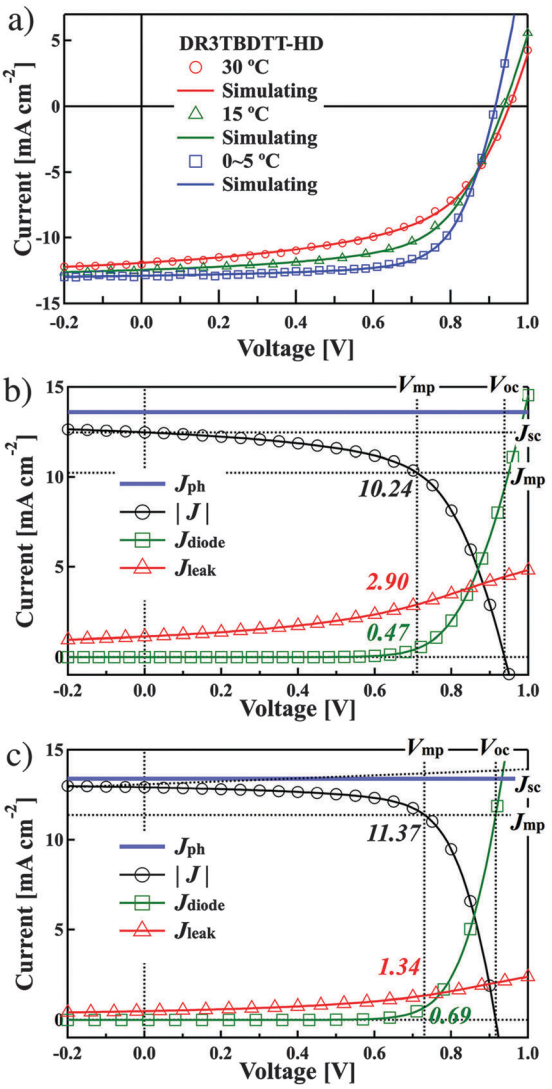

Fig. 4 (a) *J–V* characteristic curves simulating for the best devices of the DR3TBDTT-HD based solar cells under different fabrication condition. Symbols are experimental data and the lines are simulated curves. The simulation current of the best device at the spin-coating temperatures of 15 °C and 0–5 °C are presented in (b) and (c), respectively.

Table 3 Devices parameters for DR3TBDTT-HD based solar cells under different fabrication temperatures. The parameter PCE(exp) is the experimental power conversion efficiency, and the others are all simulated parameters. The best devices for 30 °C, 15 °C, and 0–5 °C are devices A13, B14, and C1, respectively. The average values are calculated from around 20 devices. More detailed data are summarized in Tables S2, S8 and S9 (ESI)

Parameter (°C)		PCE(exp) [%]	PCE [%]	V_{mp} [V]	J_{mp} [mA cm^{-2}]	V_{oc} [V]	J_{ph} [mA cm^{-2}]	C_C	$J_{diode,mp}$ [mA cm^{-2}]	$J_{leak,mp}$ [mA cm^{-2}]
30	Best	6.24	6.34	0.71	8.92	0.952	14.1	2.7	0.19	4.99
	Average	5.63	5.66	0.67	8.42	0.960	14.4	2.4	0.23	5.79
15	Best	7.21	7.27	0.71	10.24	0.938	13.6	5.3	0.47	2.90
	Average	6.93	6.96	0.71	9.84	0.942	13.9	4.3	0.41	3.61
0–5	Best	8.29	8.30	0.73	11.37	0.916	13.4	12.0	0.69	1.34
	Average	7.93	7.95	0.73	10.96	0.911	13.6	7.8	0.57	2.08

from 30 °C to 15 °C and 0–5 °C, the C_C for the best device increased from 2.7 to 5.3 and 12.0, respectively. A larger C_C led to a decreased $J_{leak,mp}$ from 4.99, 2.90 to 1.34 mA cm^{-2} and increased J_{mp} from 8.92, 10.24, 11.37 mA cm^{-2}, which greatly contributed to the device performance improvement. As a result, the average experimental PCE increased from 5.63% to 7.93%, which is an improvement of over 40%.

While for the best DR3TBDT2T based device, the C_C is as high as 12.0, and the $J_{leak,mp}$ is as small as 1.26 mA cm^{-2}, which indicated that there is not much room for DR3TBDT2T based devices to be optimized by increasing C_C, as shown in Fig. S3 and Table S10 (ESI†). For the best DR3TBDT2T based device, when lowering the spin-coating temperature to 15 °C, the C_C increased from 12.0 to 13.7 and the $J_{leak,mp}$ decreased slightly from 1.26 to 1.04 mA cm^{-2}. However, owing to the forming larger crystal size under low temperature, the J_{mp} slightly decreased from 11.25 to 10.80 mA cm^{-2}. Thus, the PCE did not increase but decreased from 8.33% to 8.14% under the low temperature spinning coating conditions. The average experimental PCE decreased from 8.02% to 7.84%. The results demonstrate that device optimization is a tricky and balanced process.

Conclusions

We observed the performance difference of DR3TBTT-HD and DR3TBDT2T based photovoltaic devices, and analysed these devices by modelling their current–voltage characteristics. A modified 2-diode model with the Hecht equation was built especially for our device system. The simulation results reveal that the poor performance of the DR3TBDTT-HD based devices was due to their larger leakage current at the maximum power point, which originated from their insufficient charge transport abilities. Raman and GI-WAXD studies supported the simulation results, showing that compared to DR3TBDT2T based films, DR3TBTT-HD based blend films exhibit a lower crystallinity. In order to suppress the current losses in DR3TBDTT-HD based devices, their active layers were spin-coated at a lower spin-coating temperature to increase their crystallinity and charge transport ability. As a result, the average experimental PCE of DR3TBTT-HD based solar cells increased by over 40%. Our work here indicates that model simulation of current–voltage characteristics is a very useful tool for photovoltaic device analysis, which could provide useful information that determines device performance. Then, corresponding device optimization can be conducted according to the simulation results and higher device performances are expected. Furthermore, through systematic study of equivalent circuit models with the help of mathematical methods, we can develop more accurate models and parameters, which could have a direct correlation with the experimental performance. We believe the OPV device optimizing process will be more effective in the near future.

Acknowledgements

The authors gratefully acknowledge financial support from MOST (Grants 2014CB643502), NSFC (Grants 51422304, 51373078 and 91433101), PCSIRT (IRT1257), and NSF of Tianjin city (13RCGFGX01121), and thank Beamline BL14B1 (Shanghai Synchrotron Radiation Facility) for providing beam time.

References

1 J. Roncali, *Acc. Chem. Res.*, 2009, **42**, 1719–1730.
2 F. C. Krebs, J. Fyenbo and M. Jørgensen, *J. Mater. Chem.*, 2010, **20**, 8994–9001.
3 Y. Sun, G. C. Welch, W. L. Leong, C. J. Takacs, G. C. Bazan and A. J. Heeger, *Nat. Mater.*, 2011, **11**, 44–48.
4 R. F. Service, *Science*, 2011, **332**, 293.
5 Y. Li, *Acc. Chem. Res.*, 2012, **45**, 723–733.
6 A. Loiudice, A. Rizzo, L. De Marco, M. R. Belviso, G. Caputo, P. D. Cozzoli and G. Gigli, *Phys. Chem. Chem. Phys.*, 2012, **14**, 3987–3995.
7 V. Gupta, A. K. Kyaw, D. H. Wang, S. Chand, G. C. Bazan and A. J. Heeger, *Sci. Rep.*, 2013, **3**, 1965.
8 Y. Liu, J. Zhao, Z. Li, C. Mu, W. Ma, H. Hu, K. Jiang, H. Lin, H. Ade and H. Yan, *Nat. Commun.*, 2014, **5**, 5293.
9 B. Kan, Q. Zhang, M. Li, X. Wan, W. Ni, G. Long, Y. Wang, X. Yang, H. Feng and Y. Chen, *J. Am. Chem. Soc.*, 2014, **136**, 15529–15532.
10 S. Zhang, L. Ye, W. Zhao, B. Yang, Q. Wang and J. Hou, *Sci. China: Chem.*, 2015, **52**, 248–256.
11 J. Chen, C. Cui, Y. Li, L. Zhou, Q. Ou, C. Li, Y. Li and J. Tang, *Adv. Mater.*, 2014, **27**, 1035–1041.
12 Z. He, C. Zhong, S. Su, M. Xu, H. Wu and Y. Cao, *Nat. Photonics*, 2012, **6**, 593–597.
13 Y. Liu, C. C. Chen, Z. Hong, J. Gao, Y. M. Yang, H. Zhou, L. Dou, G. Li and Y. Yang, *Sci. Rep.*, 2013, **3**, 3356.
14 L. Lu and L. Yu, *Adv. Mater.*, 2014, **26**, 4413–4430.

15 C. Li, C. Chang, Y. Zang, H. Ju, C. Chueh, P. Liang, N. Cho, D. S. Ginger and A. K. Y. Jen, *Adv. Mater.*, 2014, **26**, 6262–6267.
16 C. D. Wessendorf, G. L. Schulz, A. Mishra, P. Kar, I. Ata, M. Weidelener, M. Urdanpilleta, J. Hanisch, E. Mena-Osteritz, M. Lindén, E. Ahlswede and P. Bäuerle, *Adv. Energy Mater.*, 2014, **4**, 1400266.
17 C. M. Proctor, S. Albrecht, M. Kuik, D. Neher and T. Q. Nguyen, *Adv. Energy Mater.*, 2014, **4**, 1400230.
18 J. Appelbaum and A. Peled, *Sol. Energy Mater. Sol. Cells*, 2014, **122**, 164–173.
19 Y. Li, W. Huang, H. Huang, C. Hewitt, Y. Chen, G. Fang and D. L. Carroll, *Sol. Energy*, 2013, **90**, 51–57.
20 A. Gaur and P. Kumar, *Prog. Photovolt: Res. Appl.*, 2014, **22**, 937–948.
21 V. S. Balderrama, M. Estrada, A. Cerdeira, B. S. Soto-Cruz, L. F. Marsal, J. Pallares, J. C. Nolasco, B. Iñiguez, E. Palomares and J. Albero, *Microelectron. Reliab.*, 2011, **51**, 597–601.
22 B. Mazhari, *Sol. Energy Mater. Sol. Cells*, 2006, **90**, 1021–1033.
23 J. A. Anta, J. Idigoras, E. Guillen, J. Villanueva-Cab, H. J. Mandujano-Ramirez, G. Oskam, L. Pelleja and E. Palomares, *Phys. Chem. Chem. Phys.*, 2012, **14**, 10285–10299.
24 P. Schilinsky, C. Waldauf, J. Hauch and C. J. Brabec, *J. Appl. Phys.*, 2004, **95**, 2816–2819.
25 P. R. F. Barnes, A. Y. Anderson, J. R. Durrant and B. C. O'Regan, *Phys. Chem. Chem. Phys.*, 2011, **13**, 5798–5816.
26 J. Zhou, Y. Zuo, X. Wan, G. Long, Q. Zhang, W. Ni, Y. Liu, Z. Li, G. He, C. Li, B. Kan, M. Li and Y. Chen, *J. Am. Chem. Soc.*, 2013, **135**, 8484–8487.
27 B. C. Thompson and J. M. Frechet, *Angew. Chem., Int. Ed.*, 2008, **47**, 58–77.
28 C. T. Sah, R. N. Noyce and W. Shockley, *Proc. IRE*, 1957, 1228–1257.
29 S. M. Sze and K. K. Ng, *Physics of Demiconductor Devices*, John Wiley & Sons, 2006.
30 K. Nishioka, N. Sakitani, Y. Uraoka and T. Fuyuki, *Sol. Energy Mater. Sol. Cells*, 2007, **91**, 1222–1227.
31 A. Hovinen, *Phys. Scr.*, 1994, **1994**, 175–176.
32 J. Hyvarinen and J. Karila, In New Analysis Method for Crystalline Silicon Cells, Proceedings 3rd World Conference PV Energy Conversion, IEEE:2003, 1521–1524.
33 K. Kurobe and H. Matsunami, *Jpn. J. Appl. Phys.*, 2005, **44**, 8314–8321.
34 Z. Yi, W. Ni, Q. Zhang, M. Li, B. Kan, X. Wan and Y. Chen, *J. Mater. Chem. C*, 2014, **2**, 7247–7255.
35 L. Yang, J. R. Tumbleston, H. Zhou, H. Ade and W. You, *Energy Environ. Sci.*, 2013, **6**, 316–326.
36 M. S. Kim, B. G. Kim and J. Kim, *ACS Appl. Mater. Interfaces*, 2009, **1**, 1264–1269.
37 S. S. Hegedus and W. N. Shafarman, *Prog. Photovolt: Res. Appl.*, 2004, **12**, 155–176.
38 M. Gloeckler, PhD thesis, Colorado State University, 2005.
39 P. Kumar, S. C. Jain, V. Kumar, S. Chand and R. P. Tandon, *J. Appl. Phys.*, 2009, **105**, 104507.
40 R. A. Street, M. Schoendorf, A. Roy and J. H. Lee, *Phys. Rev. B: Condens. Matter Mater. Phys.*, 2010, **81**, 205307.
41 C. Voz, J. Puigdollers, J. M. Asensi, S. Galindo, S. Cheylan, R. Pacios, P. Ortega and R. Alcubilla, *Org. Electron.*, 2013, **14**, 1643–1648.
42 R. A. Street, A. Krakaris and S. R. Cowan, *Adv. Funct. Mater.*, 2012, **22**, 4608–4619.
43 K. Heeht, *Z. Phys.*, 1932, **77**, 235–245.
44 M. Zanichelli, A. Santi, M. Pavesi and A. Zappettini, *J. Phys. D: Appl. Phys.*, 2013, **46**, 365103.
45 D. S. Bale and C. Szeles, *J. Appl. Phys.*, 2010, **107**, 114512.
46 W. C. Tsoi, D. T. James, J. S. Kim, P. G. Nicholson, C. E. Murphy, D. D. Bradley, J. Nelson and J. S. Kim, *J. Am. Chem. Soc.*, 2011, **133**, 9834–9843.
47 S. Miller, G. Fanchini, Y.-Y. Lin, C. Li, C.-W. Chen, W.-F. Su and M. Chhowalla, *J. Mater. Chem. C*, 2008, **18**, 306–312.
48 Y. Liao, T. Fukuda, K. Takagi, N. Kamata, F. Fukuda and Y. Furukawa, *Thin Solid Films*, 2014, **554**, 132–136.
49 Q. Zhang, B. Kan, F. Liu, G. Long, X. Wan, X. Chen, Y. Zuo, W. Ni, H. Zhang, M. Li, Z. Hu, F. Huang, Y. Cao, Z. Liang, M. Zhang, T. P. Russell and Y. Chen, *Nat. Photonics*, 2014, **9**, 35–41.
50 F. Liu, Y. Gu, X. Shen, S. Ferdous, H. W. Wang and T. P. Russell, *Prog. Polym. Sci.*, 2013, **38**, 1990–2052.
51 G. Li, Y. Yao, H. Yang, V. Shrotriya, G. Yang and Y. Yang, *Adv. Funct. Mater.*, 2007, **17**, 1636–1644.
52 G. Lu, L. Li and X. Yang, *Small*, 2008, **4**, 601–606.
53 Y. Yao, J. Hou, Z. Xu, G. Li and Y. Yang, *Adv. Funct. Mater.*, 2008, **18**, 1783–1789.
54 Y. Sun, J.-g. Liu, Y. Ding and Y.-c. Han, *Chin. J. Polym. Sci.*, 2013, **31**, 1029–1037.
55 L. F. Lai, J. A. Love, A. Sharenko, J. E. Coughlin, V. Gupta, S. Tretiak, T. Q. Nguyen, W. Y. Wong and G. C. Bazan, *J. Am. Chem. Soc.*, 2014, **136**, 5591–5594.